



Molecular modeling and molecular dynamics simulation studies on pyrrolopyrimidine-based α -helix mimetic as dual inhibitors of MDM2 and MDMX

Shao-Yong Lu^a, Yong-Jun Jiang^{b,*}, Jian-Wei Zou^b, Tian-Xing Wu^a

^a Department of Chemistry, Zhejiang University, Hangzhou, Zhejiang 310027, PR China

^b Key Laboratory for Molecular Design and Nutrition Engineering, Ningbo Institute of Technology, Zhejiang University, Ningbo 315104, PR China

ARTICLE INFO

Article history:

Received 23 May 2011

Received in revised form 7 July 2011

Accepted 8 July 2011

Available online 19 July 2011

Keywords:

MDM2

MDMX

p53

Molecular dynamics simulations

Molecular docking

ABSTRACT

Inhibition of the interactions between the tumor suppressor protein p53 and its negative regulators, the MDM2 and MDMX oncogenic proteins, is increasingly gaining interest in cancer therapy and drug design. In this study, we carry out molecular docking, molecular dynamics (MD) simulations, and molecular mechanics Poisson-Boltzmann and generalized Born/surface area (MM-PB/GBSA) binding free energy calculations on an active compound **3a** and an inactive compound NC-1, which share a common pyrrolopyrimidine-based scaffold. MD simulations and MM-PB/GBSA calculations show that the compound NC-1 may not bind to MDM2 and MDMX, in agreement with the experimental results. Detailed MM-PB/GBSA calculations on the MDM2-**3a** and MDMX-**3a** complexes unravel that the binding free energies are similar for the two complexes. Furthermore, the van der Waals energy is the largest component of the binding free energy for both complexes, which indicates that the interactions between the compound **3a** and MDM2 and MDMX are dominated by shape complementarity. In addition, the analysis of individual residue contribution and protein–ligand binding mode show that the three functional groups on R₁, R₂, and R₃ of the compound **3a** can mimic the spatial orientation of the side chains of Phe19, Trp23, and Leu26 of p53, respectively. The obtained computational results suggest that the compound **3a** can act as a dual inhibitor of MDM2–p53 and MDMX–p53 interactions, consistent with the experimental results.

© 2011 Elsevier Inc. All rights reserved.

1. Introduction

The tumor suppressor protein p53, “the guardian of the genome”, plays a pivotal role in the regulation of cell cycle, apoptosis, and DNA repair, and is crucial for protecting the organism from cancer [1–3]. Indeed, approximately 50% of human cancers are caused by mutations or deletions of alleles in p53 [1–5]. In the remaining 50% of human cancers, p53 retains its wild-type p53 form, but its activity is effectively inhibited by its negative inhibitors, the MDM2 and MDMX oncogenic proteins. MDM2, the most extensively studied p53 activators, acts as an E3 ubiquitin ligase that promotes ubiquitin-dependent proteasomal degradation of p53 [6,7]. MDMX, a high homology to MDM2 that lacks E3 ubiquitin ligase activity, has only recently emerged as an independent regulator of p53 activation [8,9]. It abrogates p53-induced growth inhibitory and apoptotic response by inactivating the p53 transcriptional activity. Many studies have demonstrated that MDM2 and MDMX form the protein–protein interactions with the N-terminal trans-activation domain of p53 (residues 15–29),

thereby blocking the p53 transcriptional activity [10–12]. Reactivation of the p53 function by disruption of the MDM2–p53 and/or MDMX–p53 interaction has therefore become a promising therapeutic strategy for anticancer therapy across a broad spectrum of cancers.

Amplification or overexpression of MDM2 has been reported to occur in ~11% of all tumors and observed at higher levels in certain tumor types including hepatocellular carcinoma (44%), osteosarcomas (20%), and some soft tissue sarcomas (31%) [2,13]. MDMX is overexpressed or amplified in 10–20% of human cancers including breast, stomach, colon, and lung cancers and in 65% of retinoblastomas [14,15]. These evidences support the notion that the development of dual inhibitors of the MDM2 and MDMX should result in more effective anticancer drug design.

The interactions of the N-terminal trans-activation domain of p53 with the N-terminal domains of MDM2 and MDMX are well established in structural biology. X-ray crystal structures of p53–MDM2 (PDB ID: 1YCR) [10] and p53–MDMX (PDB ID: 3DAB) [12] complexes display that the short amphipathic α -helix formed by the 17–29 and 17–28 residues of p53, respectively, binds to the hydrophobic clefts of MDM2 and MDMX. The side chains of the three hydrophobic residues of p53, Phe19, Trp23, and Leu26, insert deeply into the corresponding hydrophobic clefts of MDM2

* Corresponding author. Tel.: +86 574 88229516; fax: +86 574 88229516.

E-mail address: yjjiang@nit.zju.edu.cn (Y.-J. Jiang).

and MDMX. Experimental and computational studies have revealed that the three residues are responsible for the majority of the binding free energy in the p53 [10,16–19]. Therefore, the triad of p53 residues comprises the “hot spot” of the p53–MDM2 and p53–MDMX interactions and should be critical residues to consider in the drug design. In fact, many drug candidates, such as peptides [20,21], peptidomimetics [22,23], and small molecular inhibitors [24–27], are designed to mimic the side chains of Phe19, Trp23, and Leu26.

A detailed delineation of peptide- and peptidomimetic-based inhibitors on the basis of sequence of the p53 domain to modulate the p53–MDM2 and p53–MDMX interactions has been reported elsewhere [20,28,29]. Compared with the peptide- and peptidomimetic-based inhibitors, non-peptide small molecular inhibitors have advantages in terms of water solubility, desirable oral bioavailability, and cell permeability. The X-ray crystal structures of the p53–MDM2 and p53–MDMX complexes elucidate that the majority of the p53–MDM2 and p53–MDMX interactions involve just three hydrophobic residues of p53, which are buried in a well-defined hydrophobic surface clefts of MDM2 and MDMX. Thus, it is suitable to design the small molecular inhibitors to disrupt the protein–protein interactions and subsequently to occupy the hydrophobic clefts of MDM2 and MDMX [24,30]. The current efforts have been concentrated on combinatorial library search for and structure-based de novo design of small molecular inhibitors that target the N-terminal p53-binding domains of MDM2 and MDMX.

Of the small molecular inhibitor series described to date, several classes, the cis-imidazolines (nutlins) [24], benzodiazepinediones [25], spiro-oxindoles (MI-63) [26], isoindolinone [27], as shown in Fig. 1, are able to disrupt the p53–MDM2 binding with low nanomolar affinity and specificity. These compounds, however, are only weaker inhibitors of the p53–MDMX interaction. The difference of binding affinity between two proteins is mainly attributed to the fact that the Leu26 subpocket in the p53-binding cleft is slightly smaller in MDMX than in MDM2 [31]. The two proteins have very similar secondary and tertiary structure, yet the presence of a unique and conformationally constrained Pro95–Ser96–Pro97 sequence in MDMX at the start of the $\alpha 2'$ helix, which brings Tyr99 into close proximity of the larger Met55, thereby leads to partial obstruction of the p53 binding cleft. This finding is highly supported by a recent computational comparison of MDM2 and MDMX [32–35]. Thus, the Leu26 subpocket, as suggested by Popowicz et al. [36], poses the greatest challenge for the design of dual MDM2 and MDMX inhibitors.

Recently, Popowicz et al. [36] reported the first X-ray crystal structure of MDMX bound to a small molecule inhibitor based on the 3-imidazolyl-indoles scaffold, designated as WK298 (Fig. 1). A similar small molecule inhibitor, termed WK23 (Fig. 1), was also crystallized with MDM2 to allow a direct comparison of structural differences in the two complexes. The compound WK298 binds to MDMX in a similar way that mimics parts of the p53 binding, which provides in-depth insight into a small molecule interaction with MDMX as well as provides the molecular basis for structure-based design of dual MDM2 and MDMX inhibitors.

In the very recent work, Lee et al. [37] reported the design of a novel pyrrolopyrimidine-based α -helix mimetics through a high-throughput screen. Two most active compounds, **3a** and **3b** (Fig. 1), were identified. Their observations indicate that the two compounds can serve as dual inhibitors of p53–MDM2 and p53–MDMX interactions. However, a pyrrolopyrimidine-based scaffold derivative, termed as NC-1 (Fig. 1), which has a methyl sulfonyl moiety attached to the pyrimidine ring in the compound NC-1 compared to an indolyl group attached to the same site in the compound **3a** (R_1 group), shows neither inhibition of p53–MDM2 interaction nor inhibition of p53–MDMX interaction. Elucidation of the

protein–ligand interaction at the atomic level of this group of compounds is the necessary step to obtain the dual-specific MDM2 and MDMX inhibitors with better potency. The detailed mode of mechanism as dual inhibitors and why the compound NC-1 cannot inhibit the p53–MDM2 and p53–MDMX interactions, however, are not entirely understood.

In the present study, computational studies including molecular docking, molecular dynamics (MD) simulations, molecular mechanics Poisson–Boltzmann and generalized Born/surface area (MM-PB/GBSA) binding free energy calculations are conducted to better understand the molecular basis for the binding. In addition, the decomposition of free energy on per-residue and the structural analysis are carried out to gain insights into the binding mechanism.

2. Materials and computational methods

2.1. System setups

As shown in Fig. 1, the three functional groups on R_1 , R_2 , and R_3 of the compound **3a** are more closely similar to the side chains of Phe19, Trp23, and Leu26 of p53, respectively. Furthermore, the compounds NC-1 and **3a** mainly differ in the substituent group attached on the R_1 group. Therefore, the compounds NC-1 and **3a** are selected in order to elucidate the different ligand binding mechanisms.

The structures of the compounds **3a** and NC-1 were constructed using the SYBYL [38] molecular modeling software and were energy-minimized with the Tripos force field. The crystal structures of N-terminal domains of human MDM2 and MDMX complexed with the p53 trans-activation domain were extracted from the Protein Data Bank (PDB) (PDB ID: 1YCR for p53–MDM2 complex [10]; PDB ID: 3DAB for p53–MDMX complex [12]) (<http://www.rcsb.org/pdb/>).

2.2. Molecular docking

Molecular docking of the compounds **3a** and NC-1 to the active sites of MDM2 and MDMX was carried out using the AutoDock4.2 software package, which uses a semiempirical free energy force field to evaluate conformations during docking simulations. Polar hydrogen atoms were added by using the Hydrogen module in AutoDock Tools (ADT) for MDM2 and MDMX, respectively. After that, Kollman united atom partial charges were assigned for the two proteins and the AutoDock atom types were defined using ADT. For the compounds **3a** and NC-1, all hydrogen atoms were added and the default root, rotatable bonds, and torsion of the inhibitors were set through TORSDOF module in ADT. The numbers of grid points in x , y , and z direction were set to 60, 60, and 60 with the spacing value equivalent to 0.375 Å with the help of AutoGrid. The grid center was defined at the center of the Trp23 of the p53 peptide. The distance-dependent function of the dielectric constant was employed to calculate the energetic maps.

The Lamarckian genetic algorithm (LGA) [39,40] was used for inhibitors conformational search with the following settings: a maximum number of 2,500,000 energy evaluations, an initial population of 150 randomly placed individuals, a maximum number of 27,000 generations, a mutation rate of 0.02, a crossover rate of 0.80, and an elitism value of 1. For the local search, the so-called Solis and Wets algorithm was applied with a maximum of 300 iterations per search. The docking parameters were set the same as those of our previous studies [41–43]. Other parameters were kept as the default values implemented in the program. Finally, 50 independent docking runs were carried out for each inhibitor. The docked conformations of each inhibitor were ranked into clusters based on the binding energy. Results were clustered using a tolerance of 2.0 Å

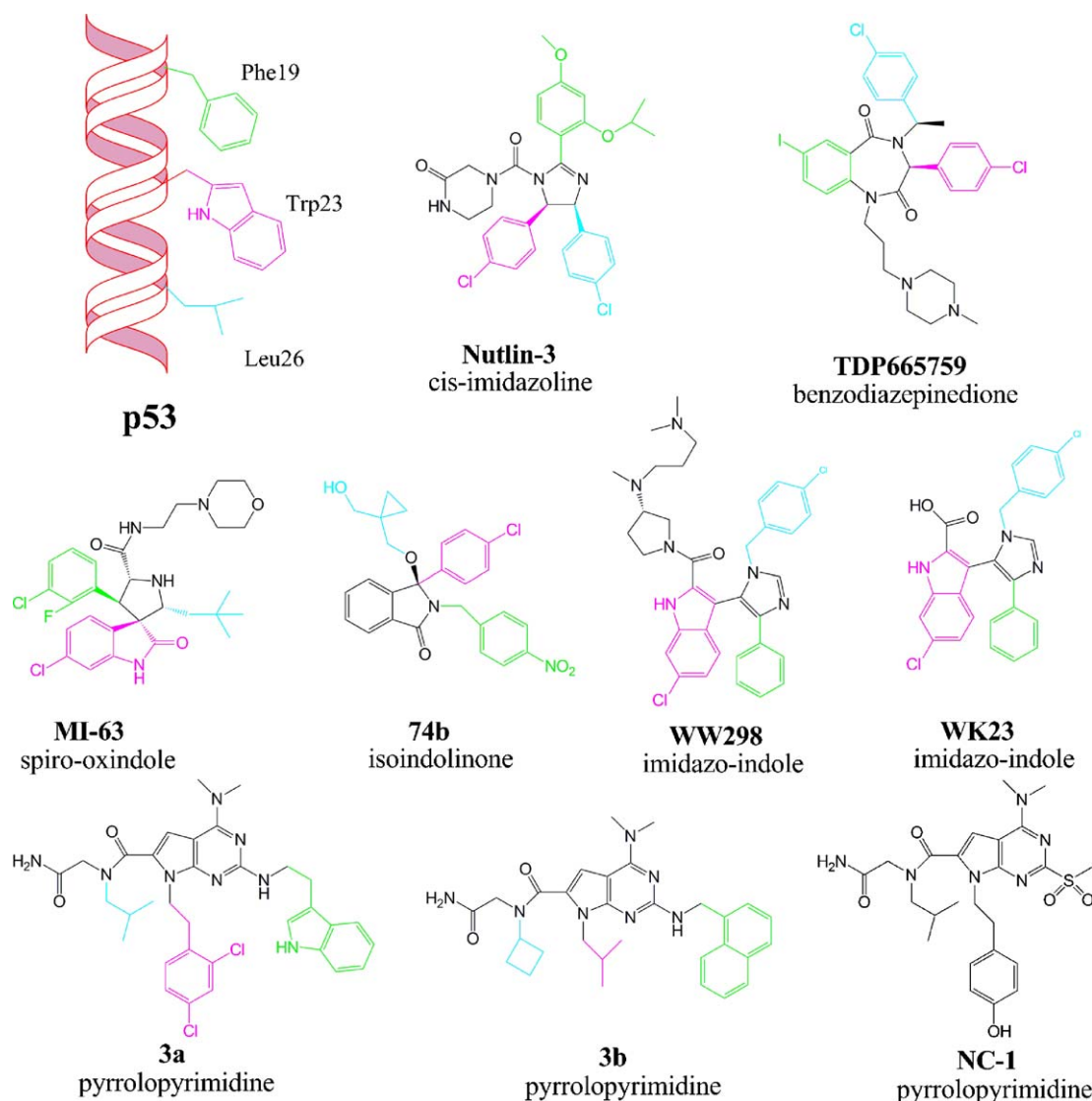


Fig. 1. α -Helix of p53 with Phe19, Trp23, and Leu26 side-chain positions and chemical structures of potent mono or dual small molecule p53–MDM2/MDMX interaction inhibitor compounds together with an inactive compound (NC-1). The functional groups that interact with the Phe19, Trp23, and Leu26 subpockets of the p53-binding cleft of MDM2 and MDMX are shown in green, magenta, and cyan, respectively. (For interpretation of the references to color in this figure legend, the reader is referred to the web version of the article.)

root-mean-square deviation (RMSD). The best docked complexes were selected in the following MD simulations.

2.3. Molecular dynamics (MD) simulations

Four MD simulations, MDM2–**3a**, MDM2–NC-1, MDMX–**3a**, and MDMX–NC-1 complexes were performed using the AMBER9 package [44]. The hydrogen atoms were added to the heavy atoms of the proteins using the Xleap module in the AMBER9 suite of program. The proteins were modeled using the AMBER FF03 force field [45], while the compounds **3a** and NC-1 were modeled using the generalized AMBER force field (GAFF) [46,47]. Partial charges on the inhibitors were calculated with the RESP HF/6-31G* method using the Antechamber encoded in AMBER9 and Gaussian03 [48]. A truncated octahedral box of TIP3P waters [49] was added with a 10 Å buffer around the complex. An appropriate number of Cl[−] counter-ions was added to maintain the electroneutrality of each system.

Energy minimizations and MD simulations were performed for each system using the SANDER module of the AMBER9 package.

First, energy minimization of the water molecules and counter-ions with gradual descent of positional restraints of 500, 300, 100, 50, 10, and 2 kcal/(mol Å²) on the protein and ligand atoms in the six steps was performed to remove the bad contacts. Each step was done with the steepest descent method for the first 1000 cycles and then the conjugated gradient method for the subsequent 1000 cycles. Afterward, the whole system was minimized without any restraint, which was done with the steepest descent method for the first 2500 cycles and then the conjugated gradient method for the subsequent 2500 cycles. After relaxation, each system was gradually heated from 0 to 150 K, and then from 150 to 300 K in 10 ps. This was followed by constant temperature equilibration at 300 K for 200 ps, with a positional restraint of 10 kcal/(mol Å²) in the complex in a canonical ensemble (NVT). Finally, 10 ns MD simulations were carried out for each system in an isothermal isobaric ensemble (NPT) with periodic boundary conditions. An integration step of 2 fs was set for the MD simulations, and the long-range electrostatic interactions were treated by the particle mesh Ewald method [50], using a cubic fourth-order B-spline interpolation, and by setting the direct sum tolerance to 10^{−5}. A cut-off equal to 10 Å

was used for short-range electrostatics and van der Waals interactions. The SHAKE method [51], with a tolerance of 10^{-5} Å, was applied to constrain all covalent bonds involving hydrogen atoms. Each simulation was coupled to a 300 K thermal bath at 1.0 atm (1 atm = 101.3 kPa) by applying the Langevin algorithm [52]. The temperature and pressure coupling parameters were set as 1 ps. The coordinates were saved every 1.0 ps for analysis.

2.4. MM-PB/GBSA calculations

Binding free energies were calculated using the MM-PB/GBSA approaches [53–58] to highlight the electrostatic and van der Waals contributions in the binding of inhibitors with the proteins. A total of 101 snapshots were extracted from the last 1 ns trajectory with an interval of 10 ps for each system. The water molecules and counter-ions were stripped. Briefly, the binding free energy ($\Delta G_{\text{binding}}$) is calculated using Eq. (1).

$$\Delta G_{\text{binding}} = \Delta G_{\text{complex}} - [\Delta G_{\text{protein}} + \Delta G_{\text{ligand}}] \quad (1)$$

Each free energy term in Eq. (1) is computed as a sum of the gas phase molecular mechanical energy (ΔE_{gas}), the solvation free energy ($\Delta G_{\text{solvation}}$) and the entropy term ($-T\Delta S$), using Eq. (2):

$$\Delta G_{\text{binding}} = \Delta E_{\text{gas}} + \Delta G_{\text{solvation}} - T\Delta S \quad (2)$$

ΔE_{gas} can be divided into contributions from the van der Waals energy (ΔE_{vdW}), electrostatic energy (ΔE_{ele}), and internal energy (ΔE_{int}) in the gas phase [Eq. (3)].

$$\Delta E_{\text{gas}} = \Delta E_{\text{vdW}} + \Delta E_{\text{ele}} + \Delta E_{\text{int}} \quad (3)$$

The solvation free energy, $\Delta G_{\text{solvation}}$, estimated using continuum solvent methods, can be partitioned into two parts [Eq. (4)]: the polar contribution ($\Delta G_{\text{PB/GB}}$) and the nonpolar contribution ($\Delta G_{\text{nonpolar}}$).

$$\Delta G_{\text{solvation}} = \Delta G_{\text{PB/GB}} + \Delta G_{\text{nonpolar}} \quad (4)$$

The electrostatic solvation energy was determined using the finite difference PB or GB model. The dielectric constants used for the interior (solute) and exterior (water) were 1 and 80, respectively. Atomic radii and charges were the same as those used in the MD simulations. The nonpolar contribution ($\Delta G_{\text{nonpolar}}$) to the solvation free energy was calculated from the solvent-accessible surface-area [Eq. (5)],

$$\Delta G_{\text{nonpolar}} = \gamma \times \text{SASA} + b \quad (5)$$

where SASA is the solvent-accessible surface-area. The corresponding solvation parameters γ and b are 0.00542 kcal/(mol Å²) and 0.92 kcal/mol for PB method and 0.0072 kcal/(mol Å²) and 0 kcal/mol for GB method. The probe radius of the solvent was set to 1.4 Å. The surface area SASA was computed using the Molsurf in AMBER9. The conformational entropy change upon ligand binding ($-T\Delta S$), obtained from the sum of translational, rotational, and vibrational components, were computed through a normal mode analysis with AMBER NMODE module [59]. The snapshots were first subjected to rigorous energy minimization for 50,000 steps using a distance-dependent dielectric of $4/r_{ij}$ (r_{ij} is the distance between two atoms) until the root-mean-square of the elements of the energy gradient vector is less than of 0.00001 kcal/(mol Å). Then the mass-weighted Hessian matrix for each minimized snapshot was calculated and diagonalized by using normal mode analysis. The obtained frequency of the normal mode was used to calculate the entropy. The experimental binding free energy was calculated from the inhibition constant K_i [Eq. (6)]. [K_i was first converted to the standard state concentration (N), and then it divided the N . R is the gas constant and T is 298 K in this study.]

$$\Delta G_{\text{exp}} = -RT \ln K_i \quad (6)$$

2.5. Inhibitor–residue interaction decomposition

The interaction energies were further decomposed into contributions from protein and ligand residue pairs, which can only use the MM-GBSA method. The binding energy of each residue pair consists of three terms: ΔE_{vdW} , ΔE_{ele} , and ΔG_{GBSA} . The same snapshots utilized in the MM-PB/GBSA calculations were used.

3. Results and discussion

3.1. Molecular docking analysis

Molecular docking of the compounds **3a** and NC-1 to the corresponding active sites of MDM2 and MDMX is performed to locate the potential binding modes of the two compounds. The active compound **3a** is designed as a dual inhibitor to mimic the binding modes of p53 with MDM2 and MDMX. After docking, the docked conformations for each compound are divided into groups according to a 2.0 Å root-mean-square deviation (RMSD) criterion using the Cluster module in ADT. Cluster conformation analysis is carried out to compare the RMSD of the lowest energy conformations and their RMSD to one another, to group them into families of similar conformations or “clusters”. The results indicate that the two compounds have two clusters, respectively. Moreover, the two compounds mainly take one binding conformation in the active sites of MDM2 and MDMX (90%). Additionally, AutoDock uses the binding free energy evaluation to find the best binding mode. The energy scoring values of AutoDock comprise intermolecular energy (constituted by van der Waals energy, hydrogen bonding energy, desolvation energy, and electrostatic energy), internal energy, and torsional free energy. During all these interactions, the hydrophobic interactions between ligand and proteins are predominant, because the van der Waals energy is the largest component of the binding free energy for each ligand. In general, the lower the binding free energy scoring value is, the more effective the binding of ligand to protein should be. Therefore, the predicted docked complexes are selected based on the lowest binding free energy for each ligand from the largest “clusters”. Each complex structure is subsequently subjected to an energy minimization procedure with AMBER03 force field, as described in the methodology.

Fig. 2 shows the predicted binding modes for the compounds **3a** and NC-1 within the corresponding active sites of MDM2 and MDMX. X-ray crystal structures reveal that the primary interactions between p53 and MDM2 and MDMX involve three hydrophobic residues (Phe19, Trp23, and Leu26) from a short α -helix in p53 and the hydrophobic surface clefts in MDM2 and MDMX, respectively. Those previously published small molecule inhibitors of the p53–MDM2 interaction, such as Nutlin-3 (cis-imidazoline) [24], TDP665759 (benzodiazepinedione) [25], and MI-63 (spiro-oxindole) [26], are designed to mimic the side chains of the Phe19, Trp23, and Leu26 residues in p53 and their interactions with MDM2 (Fig. 1). Therefore, we superimpose the predicted structures of the two compounds bound to MDM2 and MDMX on the crystal structures of the p53–MDM2 and p53–MDMX complexes, respectively, in order to reveal whether the three functional groups on R_1 , R_2 , and R_3 of the pyrrolopyrimidine scaffold can mimic the spatial orientation of the side chains of the triad residues in p53 peptide.

As shown in Fig. 3, the superimpositions suggest that the compound **3a** mimics the interactions of the p53 peptide to a higher degree than the compound NC-1. For example, the 2-(3-indolyl)-ethyl moiety (R_1 group) in the compound **3a**, whose NH forms a hydrogen bond with the carbonyl oxygen atom of Gln72 from MDM2 and of Gln71 from MDMX (Fig. 2A and B), respectively, occupies the hydrophobic pockets of MDM2 and MDMX and can mimic the side chain of Phe19. The 2-(2,4-dichlorophenyl)-ethyl moiety (R_2 group) sits deeply in the Trp23 subpocket and the isobutyl

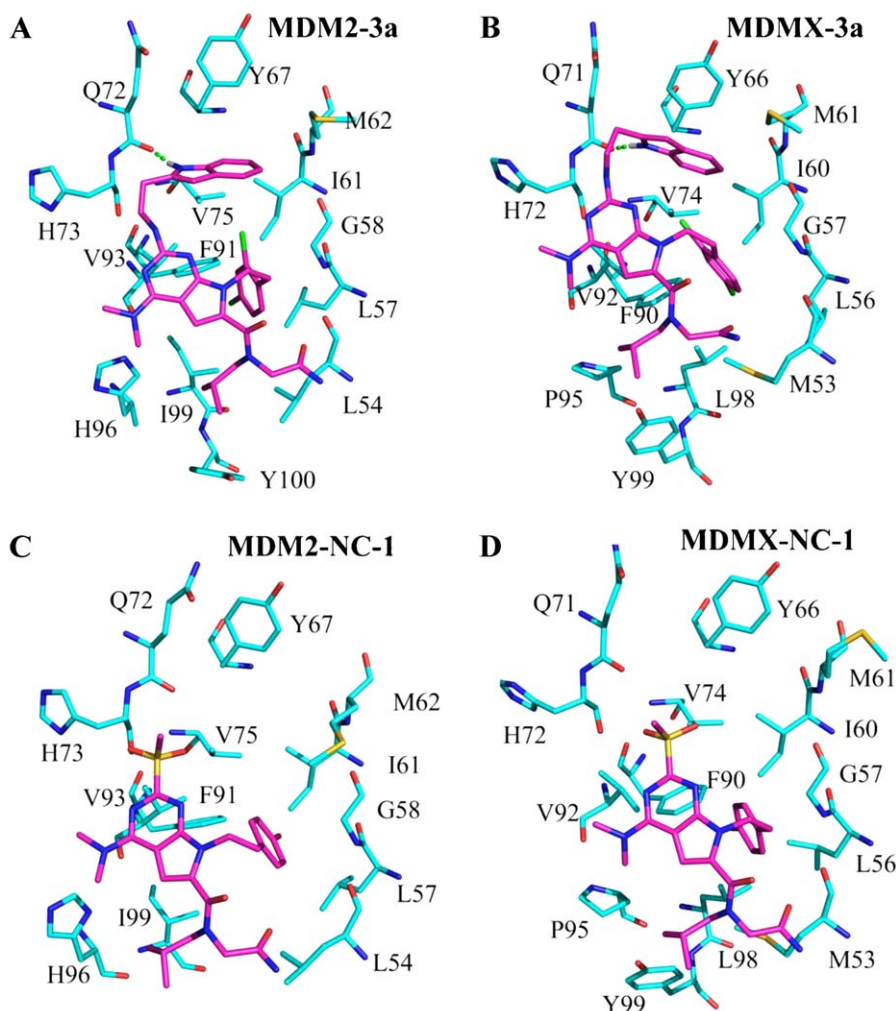


Fig. 2. (A and B) Predicted binding modes of compound **3a** in the binding sites of MDM2 and MDMX, respectively. (C and D) Predicted binding modes of compound NC-1 in the binding sites of MDM2 and MDMX, respectively. Nitrogen atoms are in blue, oxygen in red, sulfur in yellow, and chloride in green. For protein residues and ligands, carbon atoms are in cyan and magenta, respectively. Hydrogen bonds are depicted with a dashed green line. (For interpretation of the references to color in this figure legend, the reader is referred to the web version of the article.)

moiety (R_3 group) substitutes the Leu26 subpockets of MDM2 and MDMX. The pyrrolopyrimidine ring, whose primary purpose in the compound **3a** is to provide a scaffold to which all functional groups are attached. In fact, this scaffold replaces the helical backbone of the p53 peptide and is able to direct the projection of three groups into the subpockets occupied by Phe19, Trp23, and Leu26 of p53. This indicates that the compound **3a** can mimic the short α -helix in p53 to disrupt the interactions between p53 and MDM2 and MDMX. Similarly, the two functional groups on R_2 [2-(4-hydroxyphenyl)-ethyl moiety] and R_3 (isobutyl moiety) of the compound NC-1 occupy the Trp23 and Leu26 subpockets, respectively. Compared with the compound **3a**, the functional group on R_1 of the compound NC-1, however, is a methyl sulfonyl moiety, which cannot mimic the side chain of Phe19. This implies that the compound NC-1 may not stabilize in the active sites of MDM2 and MDMX. The stabilities of the compound NC-1 as well as the compound **3a** will be minutely deciphered in the MD simulations.

3.2. System stability during MD simulations

The RMSDs for all C α atoms of proteins and all heavy atoms of inhibitors relative to their initial minimized structures in the four simulated systems are monitored. As shown in Fig. 4, the fluctuations of proteins (black line) in the MDM2–**3a** (A), MDMX–**3a**

(B), and MDMX–NC-1 (D) systems follow the same trend in all cases throughout the simulations and the RMSDs tend to converge at the early stage of the simulations, with the average RMSDs of 1.0 Å for the three systems. A slight fluctuation is observed in the MDM2–NC-1 system (C) during the first 3 ns, and it then flattens out after that, with the average RMSD of 1.2 Å; this demonstrates the approaching accepted equilibrium state.

The RMSDs of the compounds **3a** and NC-1 (red line) exhibit different dynamics behaviors in the active sites of MDM2 and MDMX. The RMSD profiles of compound **3a** follow the same trend in the MDM2 (A) and MDMX (B) systems. The RMSD keeps ~ 1.0 Å during the first 4 ns. Afterward, it reaches ~ 1.5 Å in the period of 4–10 ns. This suggests that the structure of compound **3a** is relaxed during the first 4 ns MD simulations, and is equilibrated after that. Fig. 5A and B shows the superimpositions of the two periods (0–4 and 4–10 ns) of the average structures for the MDM2–**3a** and MDMX–**3a** complexes, respectively. Although the compound **3a** remains stable in the active sites of MDM2 and MDMX, it moves deeply into the hydrophobic pockets of MDM2 and MDMX in the period of 4–10 ns than in the period of 0–4 ns. The noticeable difference is observed in the R_3 group of the compound **3a**, as visualized from the superimpositions of the two periods of average structures. Fig. 5C and D shows that the R_3 group shifts from its original position and orientates deeply into the Leu26 subpockets of MDM2 and MDMX.

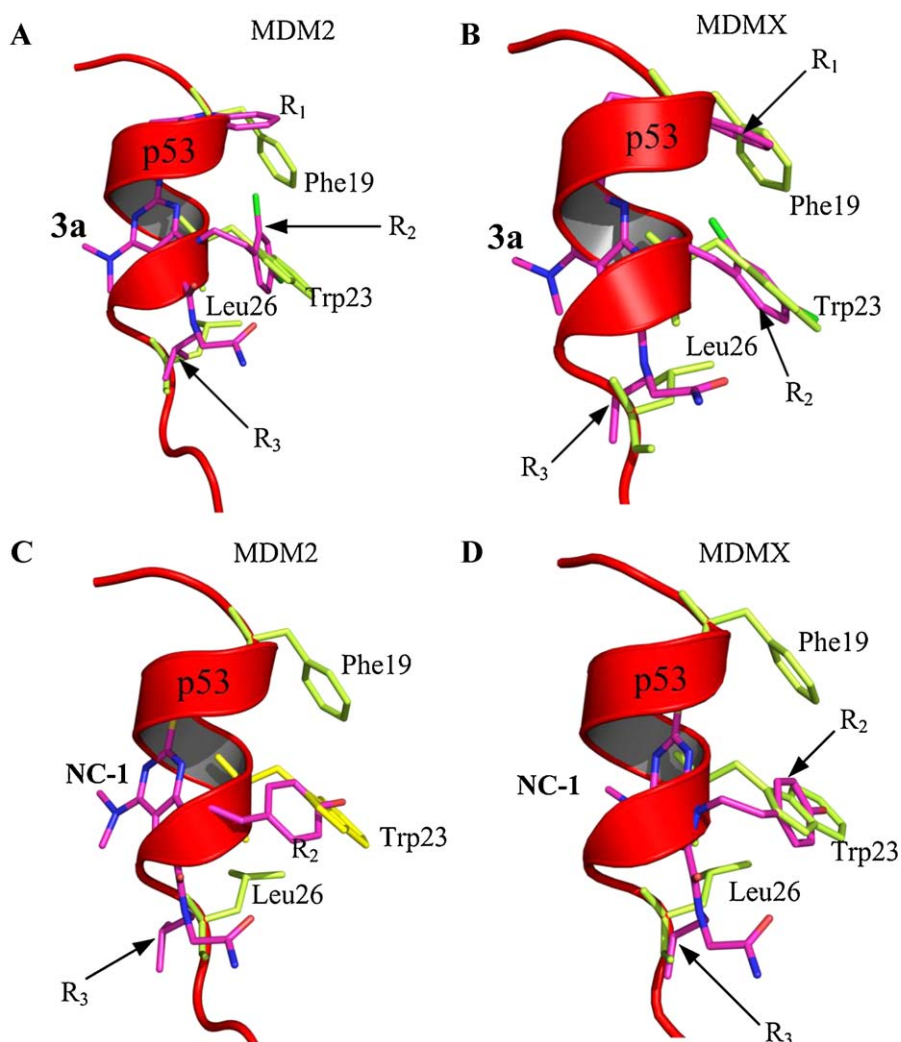


Fig. 3. (A and B) Superimpositions of the compound **3a** to the p53 peptide conformation in the crystal structures of p53 peptide complexed with MDM2 and MDMX, respectively. (C and D) Superimpositions of the compound NC-1 to the p53 peptide conformation in the crystal structures of p53 peptide complexed with MDM2 and MDMX, respectively. The p53 peptide is colored in red with cartoon representation. Three hydrophobic residues Phe19, Trp23, and Leu26 in p53 are colored in limon.

The RMSD of the compound NC-1 in MDM2 (Fig. 4C) is ~ 1.75 Å along the entire MD trajectory. In contrast, in MDMX (Fig. 4D), it increases at ~ 2.40 Å in the period of 0–4 ns, and then it converges after that. This indicates that the conformation of compound NC-1 in MDMX undergoes a notable change along the simulation. Fig. 6A and B shows the superimpositions of the average structure of the compound NC-1 from the entire 10 ns in MDM2 and from the period of 4–10 ns in MDMX to their corresponding initial minimized protein–ligand complexes. Close examination of the two overlays, it is noteworthy that the compound NC-1 is still in the hydrophobic pocket of MDM2, but it clearly moves outward of the active site. An abnormal conformational change of the compound NC-1, however, is observed in MDMX. It shows that the compound NC-1 departs from the active site of MDMX. This result has been confirmed by the experimental observation that the compound NC-1 is inactive to the p53–MDMX interaction [37]. As for the compound NC-1 in MDM2, the analysis of the binding free energy is performed to dissect its binding ability to MDM2.

3.3. Binding free energies calculations

To further examine the energetics of the compound **3a** to MDM2 and MDMX as well as the compound NC-1 to MDM2, various components of the binding free energy ($\Delta G_{\text{binding}}$) of the protein–ligand

complexes are evaluated using MM-PB/GBSA methods (Table 1). The $\Delta G_{\text{binding}}$ for the MDM2–**3a** and MDMX–**3a** complexes are significantly stronger than that for the MDM2–NC-1 complex. The total $\Delta G_{\text{binding}}$ for the MDM2–NC-1 complex is -2.23 and -3.01 kcal/mol for the MM-GBSA and MM-PBSA methods, respectively. These are approximately 12 kcal/mol higher than that of the MDM2–**3a** and MDMX–**3a** complexes. This indicates that the compound NC-1 may not bind to MDM2. Of particular interesting is observed that the calculated $\Delta G_{\text{binding}}$ of the compound **3a** to MDM2 and MDMX are identical using the MM-PB/GBSA methods, with the values of approximately -14 or -15 kcal/mol. Although there are deviations between the experimentally determined ΔG_{exp} (-8.46 kcal/mol), the general trend observed in predicted binding free energies is that the binding affinities of the compound **3a** to MDM2 and MDMX are similar. The errors in predicted binding affinities mainly come from the empirical force field parameters in AMBER for estimating binding affinity.

The free energy components responsible for the calculated binding affinities are further explored. According to the components of the $\Delta G_{\text{binding}}$ (Table 1), the favorable formations of both MDM2–**3a** and MDMX–**3a** complexes are driven by the electrostatic (ΔE_{ele}) and the van der Waals (ΔE_{vdw}) terms of the molecular mechanics energy and the nonpolar component of the solvation energy ($\Delta G_{\text{nonpolar}}$). However, the total solvation energy (ΔG_{sol}), consisted

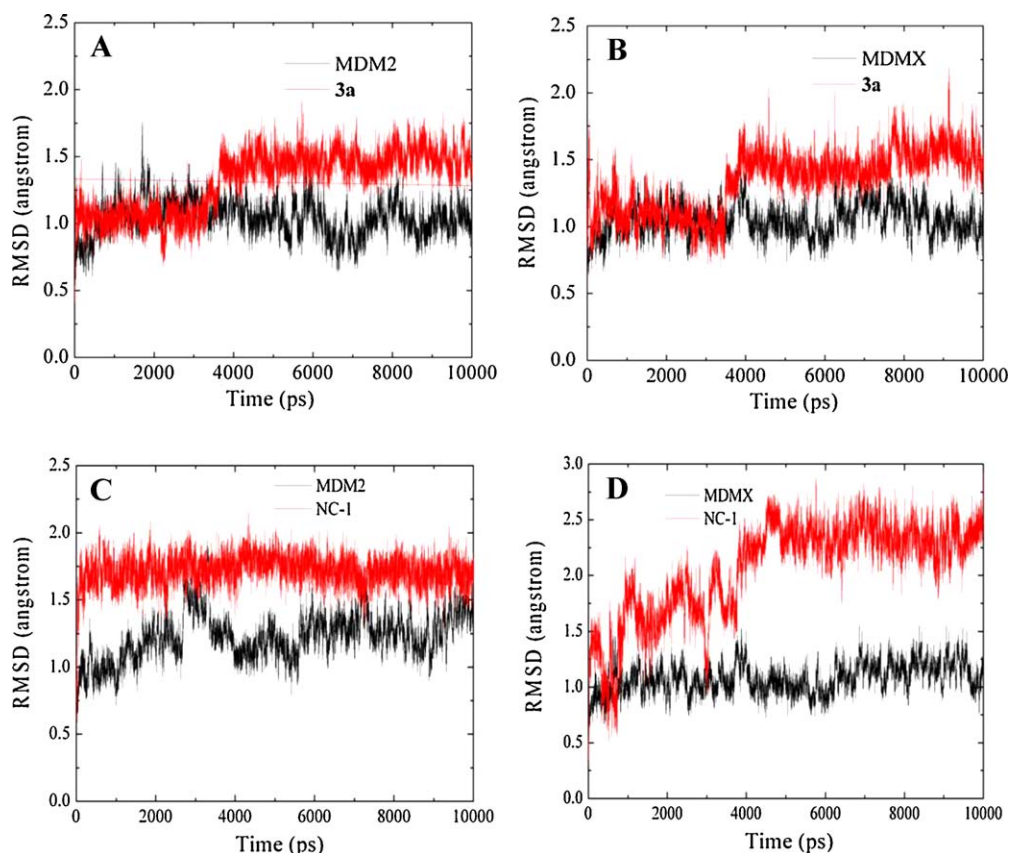


Fig. 4. The time dependence of RMSDs from the minimized structure for the C α atoms of MDM2/MDMX (black line) and the heavy atoms of inhibitors (red line) for the MDM2–**3a** (A), MDMX–**3a** (B), MDM2–NC-1 (C), and MDMX–NC-1 (D) systems in the 10 ns MD simulations. (For interpretation of the references to color in this figure legend, the reader is referred to the web version of the article.)

of polar (ΔG_{polar}) and $\Delta G_{\text{nonpolar}}$ terms, is unfavorable for both complexes. For example, the calculated ΔG_{sol} are 16.54 ± 2.64 and 20.26 ± 3.64 kcal/mol for the MDM2–**3a** and MDMX–**3a** complexes, respectively, determined by MM-PBSA method. In view of the ΔG_{sol} , it seems that the protein–ligand complexes would rather not be formed at all. Yet, the molecular mechanics energy prominently facilitates the complexes over the unbound molecules. Inspection of Table 1 reveals that for both complexes the ΔE_{vdW} interactions contribute the most to the $\Delta G_{\text{binding}}$. In line of this result, Ding

et al. [60] and Li et al. [16] also report that the p53–MDM2 and p53–MDMX binding interactions are dominated by ΔE_{vdW} interactions. This indicates that the affinities of the compound **3a** to MDM2 and MDMX are dominated by shape complementarity. This is due to that the nature of the molecular recognition of p53 is largely hydrophobic as resulting from the various hydrophobic contacts compared to polar interactions. Furthermore, the compound **3a** is designed to mimic the roles of the three hydrophobic residues (Phe19, Trp23, and Leu26) in p53. It also should be noted that the

Table 1
Free energy analysis (kcal/mol) for the binding of compounds **3a** and NC-1 to MDM2/MDMX.^a

Contribution	Complexes		
	MDM2– 3a	MDM2–NC-1	MDMX– 3a
ΔE_{ele}	–11.03 (2.86)	–20.79 (7.65)	–13.24 (3.52)
ΔE_{vdW}	–47.69 (3.46)	–34.35 (2.49)	–48.87 (3.42)
$\Delta G_{\text{nonpolar}}$ (PB)	–5.95 (0.17)	–4.87 (0.19)	–5.97 (0.20)
ΔG_{polar} (PB)	22.49 (2.73)	33.50 (6.70)	26.23 (3.71)
ΔG_{sol} (PB) ^b	16.54 (2.64)	28.63 (6.67)	20.26 (3.64)
ΔG_{ele} (PB) ^c	11.45 (2.36)	12.71 (2.11)	12.99 (2.34)
$\Delta G_{\text{nonpolar}}$ (GB)	–6.68 (0.22)	5.25 (0.25)	–6.71 (0.26)
ΔG_{polar} (GB)	23.64 (2.34)	34.65 (6.56)	24.70 (3.46)
ΔG_{sol} (GB) ^b	16.96 (2.27)	29.41 (6.53)	17.99 (3.38)
ΔG_{ele} (GB) ^c	12.61 (1.61)	13.87 (2.01)	11.46 (1.57)
$-T\Delta S$	27.03 (3.36)	23.50 (2.90)	27.89 (2.84)
$\Delta G_{\text{binding}}$ (PB/GB) ^d	–15.16 (3.15)/–14.74 (3.04)	–3.01 (2.58)/–2.23 (2.39)	–13.97 (2.84)/–14.24 (2.92)
ΔG_{exp}	–8.46	N/A ^e	–8.46

^a Numbers in the parentheses present the standard deviations. ΔE_{int} are not included here, since they are equal zero in the single trajectory approach.

^b The polar/nonpolar $\Delta G_{\text{sol}} = \Delta G_{\text{nonpolar}} + \Delta G_{\text{polar}}$ contributions.

^c The total electrostatic energy $\Delta G_{\text{ele}} = \Delta E_{\text{ele}} + \Delta G_{\text{polar}}$ contributions to the binding free energy.

^d The binding free energy ($\Delta G_{\text{binding}} = \Delta E_{\text{vdW}} + \Delta E_{\text{ele}} + \Delta G_{\text{sol}} - T\Delta S$).

^e K_i not determined.

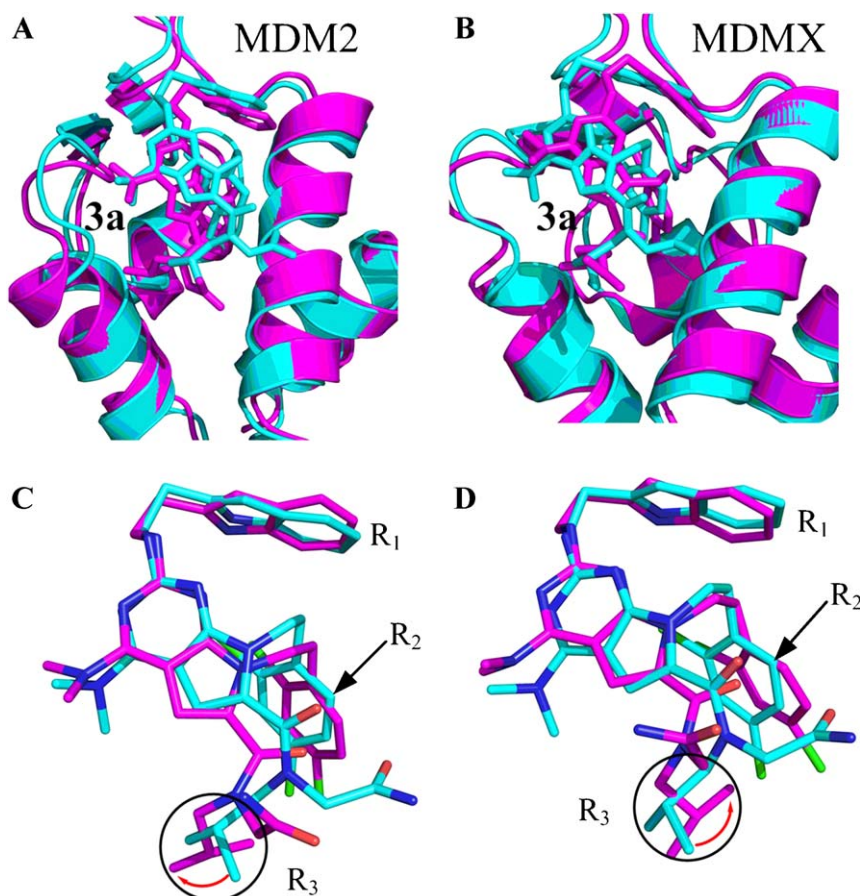


Fig. 5. The superimpositions of the backbone atoms of the average structure of MDM2–**3a** (A) and MDMX–**3a** (B) complexes in the period of 4–10 ns (magenta) to the average structure in the period of 0–4 ns (cyan). The superimpositions of the average structure of **3a** in MDM2 (C) and in MDMX (D) in the period of 4–10 ns (carbon atoms in magenta) to the average structure of **3a** in the period of 0–4 ns (carbon atoms in cyan). The red arrow shows the direction along which the motion of the R₃ group takes place. (For interpretation of the references to color in this figure legend, the reader is referred to the web version of the article.)

total electrostatic energy (ΔG_{ele}), composed of ΔE_{ele} and ΔG_{polar} , is positive for both complexes. This observation may explain that the favorable contribution of the molecular mechanics ΔE_{ele} interactions between the compound **3a** and MDM2 and MDMX is more than compensated by the electrostatic solvation free energy upon binding. Consequently, the ΔG_{ele} term contributes unfavorably to binding. This result has also been corroborated by the large body of studies [61–63], where the ΔG_{ele} between two interacting molecules disfavors their bound state over the unbound due to intense solvation forces. However, the ΔE_{ele} interactions play an important role in the formation of complexes. This notion is highly supported by a recent study reported by Macchiarulo et al. [32] that the ΔE_{ele} interactions may be presented as the directional interactions required for the mechanism of complex formation between p53 and MDM2 and MDMX.

3.4. Inhibitor–residue interaction decomposition

The $\Delta G_{\text{binding}}$ is further decomposed into individual residue contributions using MM-GBSA method for the three complexes (Fig. 7). This quantitative information is very helpful for understanding the mechanistic basis for the formation of a protein–ligand complex. The favorable residues are focused on the hydrophobic surface cleft of the N-terminal domains of MDM2 and MDMX. These residues include L54/M53, L57/L56, G58/G57, I61/I60, M62/M61, Y67/Y66, Q72/Q71, H73/H72, V75/V74, F91/F90, V93/V92, H96/P95, I99/L98, and Y100/Y99 (MDM2/MDMX residue numbering), which are in good agreement with the binding pockets of p53 peptide

in MDM2 and MDMX [18,64,65]. Table 2 lists the energy contributions of these key residues on the binding. Comparison of the MDM2–**3a** and MDMX–**3a** complexes, five residues (L54/M53, I61/I60, Q72/Q71, H73/H72, and V93/V92 for MDM2 and MDMX) contribute larger energies in both complexes and V93/V92 has the highest value for the energy contribution in MDM2 and MDMX. This is in agreement with the results of the computational alanine scanning mutagenesis study in MDM2 that only one residue, Val93,

Table 2
Energy contributions (kcal/mol) of critical residues at the hydrophobic surface cleft of MDM2/MDMX to the binding.

Residues	MDM2		Residues	MDMX
	3a	NC-1		3a
L54	−2.14	−3.38	M53	−2.03
L57	−1.01	−1.17	L56	−1.21
G58	−1.32	−0.64	G57	−1.29
I61	−1.79	−0.52	I60	−1.69
M62	−0.89	−0.17	M61	−0.71
Y67	−1.06	0.01	Y66	−0.93
Q72	−1.66	0.06	Q71	−1.81
H73	−1.69	−0.61	H72	−1.83
V75	−0.56	−0.09	V74	−0.57
F91	−0.47	−0.18	F90	−0.47
V93	−4.43	−3.07	V92	−4.44
H96	−1.01	−1.37	P95	−1.26
I99	−0.82	−1.38	L98	−1.32
Y100	−0.74	−0.37	Y99	−1.04

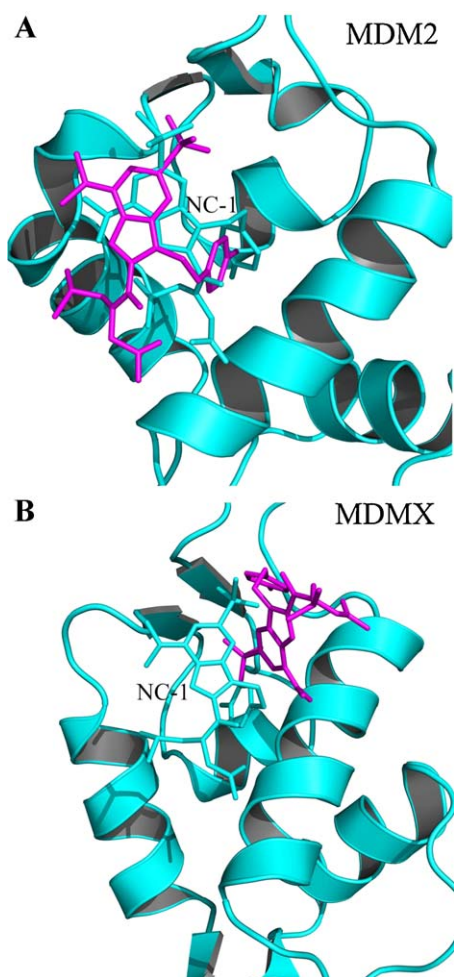


Fig. 6. The superimpositions of the average structure of the compound NC-1 from the entire 10 ns (A) (magenta) in MDM2 and from the period of 4–10 ns (B) (magenta) in MDMX to their corresponding initial minimized protein–ligand complexes (cyan). (For interpretation of the references to color in this figure legend, the reader is referred to the web version of the article.)

with a $\Delta G_{\text{binding}}$ upon alanine mutation higher than 2.0 kcal/mol is observed [66].

Comparison of individual residue contributions to the MDM2–3a and MDM2–NC-1 complexes, the different energy contributions mainly originate from Ile61, Met62, Tyr67, Gln72, His73, and Val93, which situate in the Phe19 subpocket of p53. Interestingly, the main differences between the compounds 3a and NC-1 lie in the R₁ group, which mimics the side chain of Phe19. Quantum mechanical calculations of residue-specific hydrophobic interactions in p53–MDM2 complex by Ding et al. [60] reveal that Phe19, multiple strong interactions with MDM2 residues including Met61, Tyr67, and Gln72, has larger contributions to interaction, with the total interaction energy of ~ 24 kcal/mol. Analysis of X-ray crystal structures of p53–MDM2 and p53–MDMX complexes show that the Phe19, a critical residue, of p53 peptide plays an indispensable role in the p53–MDM2 and p53–MDMX interactions, a suggestion that finds support in results from mutation analysis and alanine scanning of p53 peptides. Ala mutation of Phe19 weakens p53 binding to MDM2 and MDMX by at least 3 orders of magnitude, resulting in the abolishing the complex formation [67]. In the work of Espinoza-Fonseca and García-Machorro [68], the authors propose that the aromatic interactions between MDM2 and Phe19 and Trp23 of p53 are important, and probably essential, requirement for the formation and stabilization of the p53–MDM2 complex. Combined with the aforementioned results,

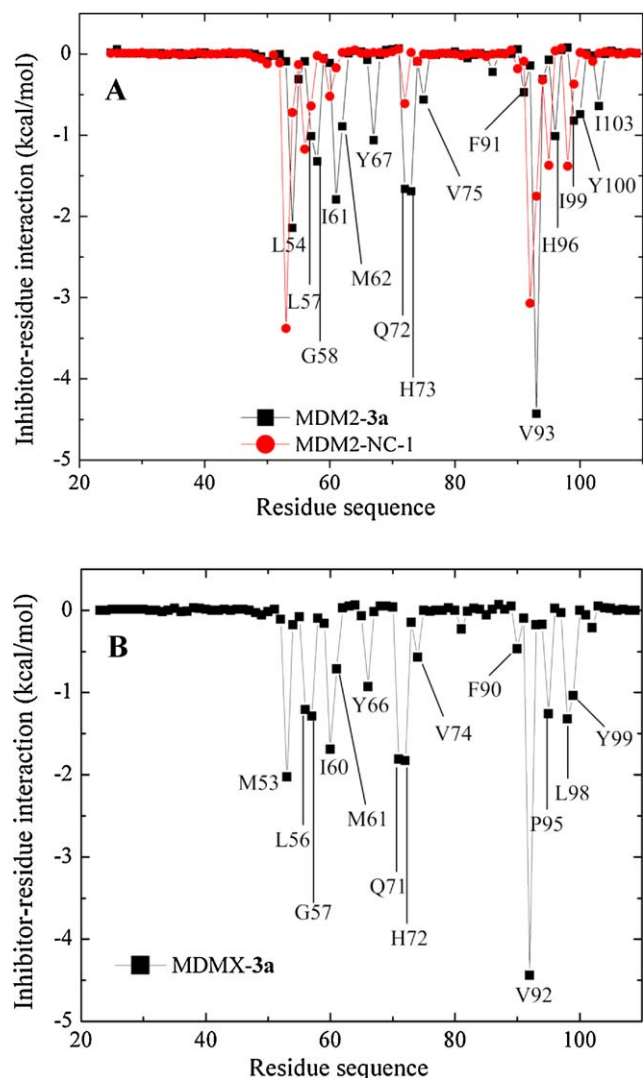


Fig. 7. Decomposition of the binding free energies on a per-residue basis for the MDM2–3a (A, black line), MDM2–NC-1 (A, red line), and MDMX–3a complexes (B). (For interpretation of the references to color in this figure legend, the reader is referred to the web version of the article.)

together with the $\Delta G_{\text{binding}}$ and individual residue contributions calculations in this work, we conclude that the compound NC-1 may not bind to MDM2.

3.5. Binding modes of MDM2–3a and MDMX–3a complexes

The individual residue decomposition of total energy gives us a better understanding and more detailed information in the interactions between the compound 3a and the hydrophobic pockets of MDM2 and MDMX. The analysis of the intermolecular interactions including hydrophobic and hydrogen-bonding contacts on the last frames of the MDM2–3a and MDMX–3a complexes is carried out using Ligplot [69], as shown in Fig. 8. The N–H of the R₁ group of the compound 3a is engaged in hydrogen bonding interaction with the backbone carbonyl group of Q72/Q71 of MDM2 and MDMX. This hydrogen bond in each complex shows high percentage of occurrence data with similar distances (2.855 ± 0.12 Å, 99.94% occurrence for MDM2; 2.844 ± 0.12 Å, 99.68% occurrence for MDMX). Comparing hydrophobic and hydrogen-bonding interactions, hydrophobic interactions, however, play a key role in stabilizing the protein–ligand interface.

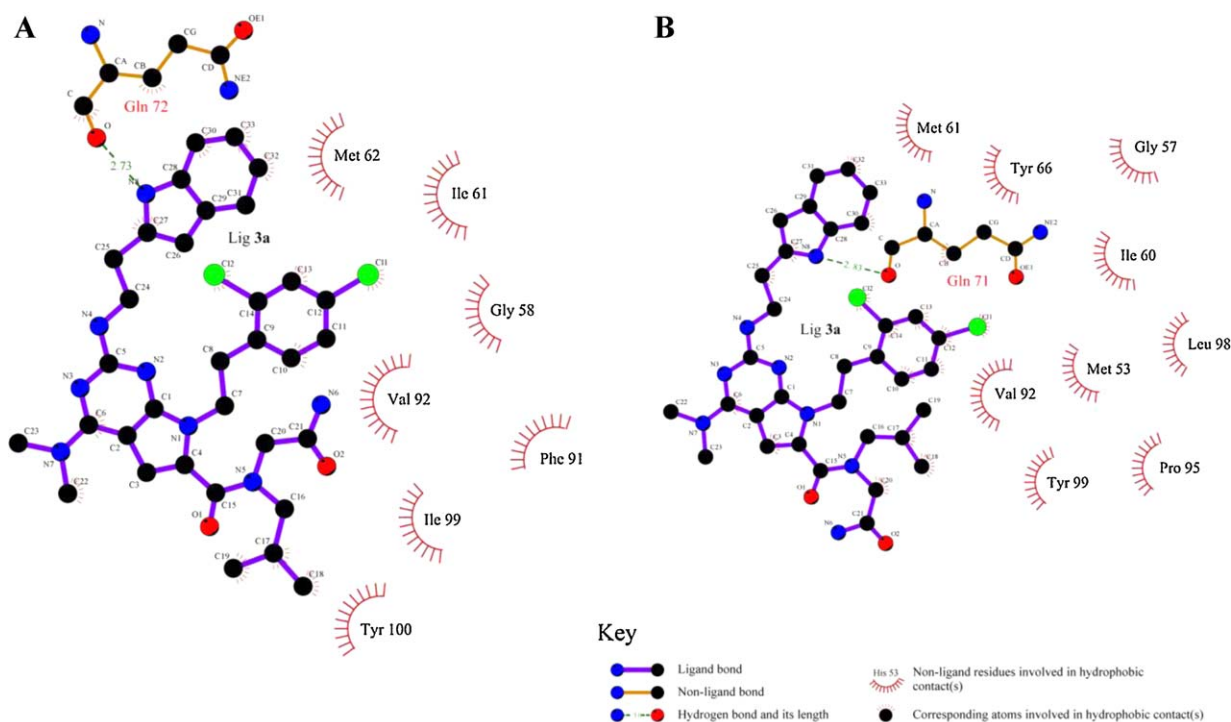


Fig. 8. Ligplot analyses result. 2D representation of ligand–protein interactions for the MDM2–**3a** (A) and MDMX–**3a** (B) complexes.

Fig. 9 illustrates the molecular surface visualizations of the two average structures in the period of 4–10 ns. It is clearly seen that the compound **3a** occupies in the hydrophobic pockets of MDM2 and MDMX. The R₁ group of compound **3a** is located inside the Phe19 subpocket formed by I61/I60, M62/M61, Y67/Y66, Q72/Q71, and V75/V74 in MDM2/MDMX. In addition, a stable hydrogen bond is formed between the N–H of the R₁ group and the backbone carbonyl Q72/Q71 in MDM2 and MDMX, as evidenced in the MD simulations. The R₂ group sits deeply in the Trp23 subpocket formed by L57/L56, G58/G57, F91/F90, V93/V92 and I99/L98 in MDM2/MDMX. The 4-Cl atom of the R₂ group protrudes into a void of the Trp23 binding sites of MDM2 and MDMX, making additional van der Waals interactions with F91/F90 and I99/L98 in MDM2 and MDMX.

Chlorinated aromatic groups that mimic the side chain of Trp23 are often observed in most of known small molecule MDM2 and MDMX inhibitors (see Fig. 1) as well as in peptidomimetic-based inhibitors such as 6-chlorotryptophane (Cl-Trp) in the 8-mer peptide analogue (Novartis peptide) [22]. Sakurai et al. [70] explain this phenomenon attributed to that chlorine has a van der Waals of 1.8 Å and there is no other organic functionality of an equivalent size, suggesting that chlorine is the idea size to fill into the cavity at the bottom of the Trp23 binding site. The noticeably different binding modes between two complexes lie in the Leu26 subpocket. The R₃ group is located inside the Leu26 subpocket formed by Leu54, Val93, His96, Ile99, and Tyr100 from MDM2. However, this binding site is formed by Met53, Val92, Pro95, Leu98, and Tyr99 from

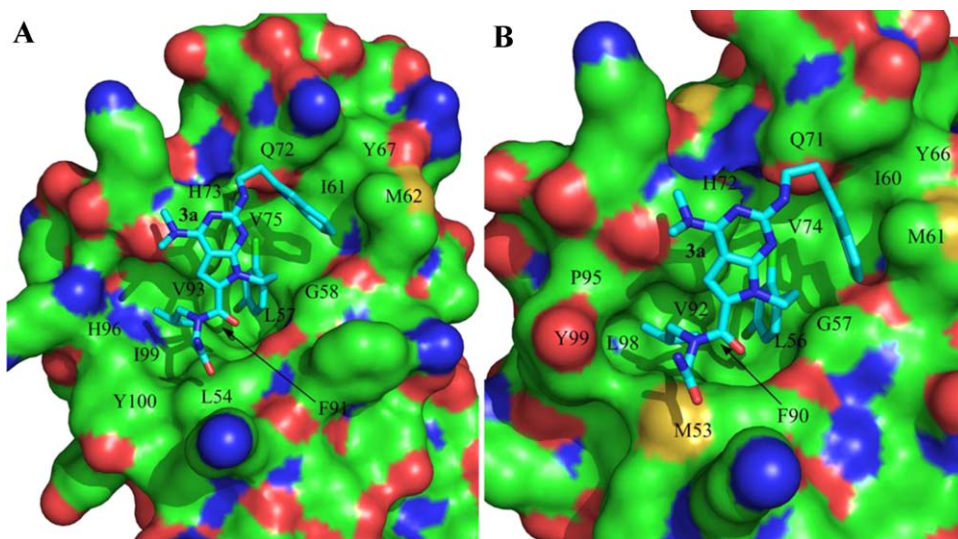


Fig. 9. Surface representations of MDM2 (A) and MDMX (B) in complex with the compound **3a**. MDM2 and MDMX are visualized with their molecular surface with surface atoms distribution: red for oxygen atoms, blue for nitrogen atoms, green for carbon atoms, and yellow for sulfur atoms. (For interpretation of the references to color in this figure legend, the reader is referred to the web version of the article.)

MDMX. It is clearly seen that the Leu26 subpocket is smaller in MDMX than in MDM2, as shown in Fig. 9. As reported by Popowicz et al. [31] the proteins MDM2 and MDMX differ significantly in the shape and properties of residues surrounding the Leu26 subpocket of p53 with this subpocket is slightly smaller in MDMX than in MDM2. A structural perspective for the designed dual MDM2 and MDMX inhibitors described by Riedinger and McDonnell [71] points out that an inhibitor that binds to MDM2 and MDMX would have to exploit the special properties of the Leu26 subpocket. The isobutyl moiety (R₃ group), identical to the side chain of Leu26 in p53, is comfortably accommodated in the Leu26 subpockets of MDM2 and MDMX evidenced in the MD simulations, supporting the hypothesis that it can act as a dual MDM2 and MDMX inhibitors. Overall, the compound **3a** binds to MDM2 and MDMX in a way that mimics the binding of the native p53 peptide.

4. Conclusions

In the present study, molecular docking, MD simulations, and MM-PB/GBSA binding free energy calculations on the compounds **3a** and NC-1 are performed to investigate the potential binding modes and to evaluate their binding affinities. The compounds **3a** and NC-1 mainly differ in the substituent group on the R₁ group. For the compound NC-1 in MDMX, MD simulation shows that it cannot stabilize in the hydrophobic cleft of MDMX. For the compound NC-1 in MDM2, the $\Delta G_{\text{binding}}$ calculation shows that the $\Delta G_{\text{binding}}$ of the compound NC-1 to MDM2 is significantly weaker than that of the compound **3a** to MDM2. Furthermore, individual residue contribution calculation reveals that the interactions between the R₁ group of the compound NC-1 and the Phe19 subpocket residues are also weak, indicating that this group cannot mimic the side chain of Phe19 of p53. Therefore, the compound NC-1 may not bind to MDM2 and MDMX, consistent with the experimental data.

MD simulations reveal that the compound **3a** is stable in the hydrophobic clefts of MDM2 and MDMX and the dynamics behaviors of the compound **3a** in the two proteins are similar. The $\Delta G_{\text{binding}}$ calculations, the decompositions of $\Delta G_{\text{binding}}$ on an individual residue, and the structural analyses show that the three functional groups on R₁, R₂, and R₃ of the compound **3a** can mimic the side chains role of Phe19, Trp23, and Leu26 of p53, respectively. The binding pockets for the compound **3a** are composed of L54/M53, L57/L56, G58/G57, I61/I60, M62/M61, Y67/Y66, Q72/Q71, H73/H72, V75/V74, F91/F90, V93/V92, H96/P95, I99/L98, and Y100/Y99 from MDM2/MDMX. Overall, the compound **3a** binds to MDM2 and MDMX in a similar fashion that mimics the binding modes of the native p53 peptide. The results obtained from this study will be valuable for future rational design of novel and potent dual MDM2 and MDMX inhibitors as promising anticancer therapeutics.

Acknowledgment

This work was supported by the Natural Science Foundation of China (No. 20803063).

References

- [1] B. Vogelstein, D. Lane, A. Levine, Surfing the p53 network, *Nature* 408 (2000) 307–310.
- [2] F. Toledo, G.M. Wahl, Regulating the p53 pathway: in vitro hypotheses, in vivo veritas, *Nat. Rev. Cancer* 6 (2006) 909–923.
- [3] K.H. Vousden, D.P. Lane, P53 in health and disease, *Nat. Rev. Mol. Cell Biol.* 8 (2006) 275–283.
- [4] M. Hollstein, D. Sidransky, B. Vogelstein, C.C. Harris, P53 mutations in human cancers, *Science* 253 (1990) 49–53.
- [5] A.C. Joerger, A.R. Fersht, Structural biology of the tumor suppressor p53, *Annu. Rev. Biochem.* 77 (2008) 557–582.
- [6] Y. Haupt, R. Maya, A. Kazaz, M. Oren, Mdm2 promotes the rapid degradation of p53, *Nature* 387 (1997) 296–299.
- [7] M.H. Kubbutat, S.N. Jones, K.H. Vousden, Regulation of p53 stability by Mdm2, *Nature* 387 (1997) 299–303.
- [8] J.C. Marine, M.A. Dyer, A.G. Jochemsen, Inactivation of the p53 pathway in retinoblastomas, *J. Cell Sci.* 120 (2007) 371–378.
- [9] M. Wade, G.M. Wahl, Targeting Mdm2 and Mdmx in cancer therapy: better living through medicinal chemistry? *Mol. Cancer Res.* 7 (2009) 1–11.
- [10] P.H. Kussie, S. Gorina, V. Marechal, B. Elenbaas, J. Moreau, A.J. Levine, N.P. Pavletich, Structure of the MDM2 oncoprotein bound to the p53 tumor suppressor transactivation domain, *Science* 274 (1996) 948–953.
- [11] J.D. Oliner, J.A. Pietenpol, S. Thiagalingam, J. Gyuris, K.W. Kinzler, B. Vogelstein, Oncoprotein MDM2 conceals the activation domain of tumor suppressor p53, *Nature* 362 (1993) 857–860.
- [12] G.M. Popowicz, A. Czarna, T.A. Holak, Structure of the human Mdmx protein bound to the p53 tumor suppressor transactivation domain, *Cell Cycle* 7 (2008) 2441–2443.
- [13] J.D. Oliner, K.W. Kinzler, P.S. Meltzer, D.L. George, B. Vogelstein, Amplification of a gene encoding a p53-associated protein in human sarcomas, *Nature* 358 (1992) 80–83.
- [14] Y.F. Ramos, R. Stad, J. Attema, L.T. Peltenburg, A.J. van der Eb, A.G. Jochemsen, Aberrant expression of HDMX proteins in tumor cells correlates with wild-type p53, *Cancer Res.* 61 (2001) 1839–1842.
- [15] N.A. Laurie, S.L. Donovan, C.S. Shih, J. Zhang, N. Mills, C. Fuller, A. Teunisse, S. Lam, Y. Ramos, A. Mohan, D. Johnson, M. Wilson, C. Rodriguez-Galindo, M. Quarto, S. Francoz, S.M. Mendrynska, R.K. Guy, J.C. Marine, A.G. Jochemsen, M.A. Dyer, Inactivation of the p53 pathway in retinoblastoma, *Nature* 444 (2006) 61–66.
- [16] C. Li, M. Pazgier, C. Li, W. Yuan, M. Liu, G. Wei, W.Y. Lu, W. Lu, Systematic mutational analysis of peptide inhibition of the p53–MDM2/MDMX interactions, *J. Mol. Biol.* 398 (2010) 200–213.
- [17] K. Barakat, J. Mane, D. Friesen, J. Tuszynski, Ensemble-based virtual screening reveals dual-inhibitors for the p53–MDM2/MDMX interactions, *J. Mol. Graph. Model.* 28 (2010) 555–568.
- [18] J. Chen, J. Wang, B. Xu, W. Zhu, G. Li, Insights into mechanism of small molecule inhibitors of the MDM2–p53 interaction: molecular dynamics simulation and free energy analysis, *J. Mol. Graph. Model.* (2011), doi:10.1016/j.jmgm.2011.06.003.
- [19] G. Hu, D. Wang, X. Liu, Q. Zhang, A computational analysis of the binding model of MDM2 with inhibitors, *J. Comput. Aided Mol. Des.* 24 (2010) 687–697.
- [20] A. Czarna, G.M. Popowicz, A. Pecak, S. Wolf, G. Dubin, T.A. Holak, High affinity interaction of the p53 peptide-analogue with human Mdm2 and Mdmx, *Cell Cycle* 8 (2009) 1176–1184.
- [21] M. Liu, C. Li, M. Pazgier, C. Li, Y. Mao, Y. Lv, B. Gu, G. Wei, W. Yuan, C. Zhan, W.Y. Lu, W. Lu, D-peptide inhibitors of the p53–MDM2 interaction for targeted molecular therapy of malignant neoplasms, *Proc. Natl. Acad. Sci. U.S.A.* 107 (2010) 14321–14326.
- [22] C. Garcia-Echeverria, P. Chène, M.J.J. Blommers, P. Furet, Discovery of potent antagonists of the interaction between human double minute 2 and tumor suppressor p53, *J. Med. Chem.* 43 (2000) 3205–3208.
- [23] A. Böttger, V. Böttger, S.F. Howard, S.M. Pickles, P. Chène, C. Garcia-Echeverria, H.K. Hochkeppel, D.P. Lane, Identification of novel mdm2 binding peptides by phage display, *Oncogene* 13 (1996) 2141–2147.
- [24] L.T. Vassilev, B.T. Vu, B. Graves, D. Carvajal, F. Podlaski, Z. Filipovic, N. Kong, U. Kammloft, C. Lukacs, C. Klein, N. Fotouhi, E.A. Liu, In vivo activation of the p53 pathway by small-molecule antagonists of MDM2, *Science* 303 (2004) 844–848.
- [25] B.L. Grasberger, T. Lu, C. Schubert, D.J. Parks, T.E. Carver, H.K. Koblish, M.D. Cummings, L.V. LaFrance, K.L. Milkiewicz, R.R. Calvo, D. Maguire, J. Lattanze, C.F. Franks, S. Zhao, K. Ramachandren, G.R. Bylebyl, M. Zhang, C.L. Manthey, E.C. Petrella, M.W. Pantoliano, I.C. Deckman, J.C. Spurlino, A.C. Maroney, B.E. Tomczuk, C.J. Molloy, R.F. Bone, Discovery and cocrystal structure of benzodiazepinedione HDM2 antagonists that activate p53 in cells, *J. Med. Chem.* 48 (2005) 909–912.
- [26] K. Ding, Y. Lu, Z. Nikolovska-Coleska, G. Wang, S. Qiu, S. Shangary, W. Gao, D. Qin, J. Stuckey, K. Krajewski, P.P. Roller, S. Wang, Structure-based design of spiro-oxindoles as potent, specific small-molecule inhibitors of the MDM2–p53 interaction, *J. Med. Chem.* 49 (2006) 3432–3435.
- [27] I.R. Hardcastle, J. Liu, E. Valeur, A. Watson, S.U. Ahmed, T.J. Blackburn, K. Ben-naceur, W. Clegg, C. Drummond, J.A. Endicott, B.T. Golding, R.J. Griffin, J. Gruber, K. Haggerty, R.W. Harrington, C. Hutton, S. Kemp, X. Lu, J.M. McDonnell, D.R. Newell, M.E.M. Noble, S.L. Payne, C.H. Revill, C. Riedinger, Q. Xu, J. Lunec, Isoindolinone inhibitors of murine double minute 2 (MDM2)–p53 protein–protein interaction: structure–activity studies leading to improved potency, *J. Med. Chem.* 54 (2011) 1233–1243.
- [28] M. Pazgier, M. Liu, G. Zou, W. Yuan, C. Li, C. Li, J. Monbo, D. Zella, S.G. Tarasov, W. Lu, Structural basis for high-affinity peptide inhibition of p53 interactions with MDM2 and MDMX, *Proc. Natl. Acad. Sci. U.S.A.* 106 (2009) 4665–4670.
- [29] C. Li, M. Pazgier, M. Liu, W.Y. Lu, W. Lu, Apamin as template for structure-based rational design of potent peptide activators of p53, *Angew. Chem. Int. Ed.* 48 (2009) 8712–8715.
- [30] M.P. Dickens, R. Fitzgerald, P.M. Fischer, Small-molecule inhibitors of MDM2 as new anticancer therapeutics, *Semin. Cancer Biol.* 20 (2010) 10–18.
- [31] G.M. Popowicz, A. Czarna, U. Rothweiler, A. Szwagierczak, M. Krajewski, L. Weber, T.A. Holak, Molecular basis for the inhibition of p53 by Mdmx, *Cell Cycle* 6 (2007) 2386–2392.

- [32] A. Macchiarulo, N. Giacchè, A. Carotti, M. Baroni, G. Cruciani, R. Pellicciari, Targeting the conformational transitions of MDM2 and MDMX: insights into dissimilarities and similarities of p53 recognition, *J. Chem. Inf. Model.* 48 (2008) 1999–2009.
- [33] A. Carotti, A. Macchiarulo, N. Giacchè, R. Pellicciari, Targeting the conformational transitions of MDM2 and MDMX: insights into key residues affecting p53 recognition, *Proteins* 77 (2009) 524–535.
- [34] L.M. Fonseca-Espinoza, J.G. Ferrara-Trujillo, Conformational changes of the p53-binding cleft of MDM2 revealed by molecular dynamics simulations, *Biopolymers* 83 (2006) 365–373.
- [35] S.G. Dastidar, D.P. Lane, C.S. Verma, Modulation of p53 binding to MDM2: computational studies reveal important roles of Tyr100, *BMC Bioinformatics* 10 (2009) S6.
- [36] G.M. Popowicz, A. Czarna, S. Wolf, K. Wang, W. Wang, A. Dömling, T.A. Holak, Structure of low molecular weight inhibitors bound to MDMX and MDM2 reveal new approaches for p53–MDMX/MDM2 antagonist drug discovery, *Cell Cycle* 9 (2010) 1104–1111.
- [37] J.H. Lee, Q. Zhang, S. Jo, S.C. Chai, M. Oh, W. Im, H. Lu, H.S. Lim, Novel pyrrolopyrimidine-based α -helix mimetics: cell-permeable inhibitors of protein–protein interactions, *J. Am. Chem. Soc.* 133 (2011) 676–679.
- [38] Sybyl Version 6.8, Tripos Associates Inc., St. Louis, MO, 2001.
- [39] G.M. Morris, R. Huey, W. Lindstrom, M.F. Sanner, R.K. Belew, D.S. Goodsell, A.J. Olson, Autodock4 and AutoDockTools4: automated docking with selective receptor flexibility, *J. Comput. Chem.* 30 (2009) 2785–2791.
- [40] H.K. Srivastava, M. Chourasia, D. Kumar, G.N. Sastry, Comparison of computational methods to model DNA minor groove binders, *J. Chem. Inf. Model.* 51 (2011) 558–571.
- [41] S.-Y. Lu, Y.-J. Jiang, J. Lv, T.-X. Wu, Q.-S. Yu, W.-L. Zhu, Molecular docking and molecular dynamics simulation studies of GPR40 receptor–agonist interactions, *J. Mol. Graph. Model.* 28 (2010) 766–774.
- [42] S.-Y. Lu, Y.-J. Jiang, J.-W. Zou, H.-B. Luo, T.-X. Wu, Insights into analysis of interactions of GW9508 to wild-type and H86F and H137F GPR40: a combined QM/MM study and pharmacophore modeling, *J. Mol. Graph. Model.* 29 (2011) 818–825.
- [43] S.-Y. Lu, Y.-J. Jiang, J.-W. Zou, T.-X. Wu, Role of bridging water molecules in GSK3 β –inhibitor complexes: insights from QM/MM, MD and molecular docking studies, *J. Comput. Chem.* 32 (2011) 1907–1918.
- [44] D.A. Case, T.A. Darden, T.E. Cheatham III, C. Simmerling, J. Wang, R.E. Duke, R. Luo, K.M. Merz, D.A. Pearlman, M. Crowley, R.C. Walker, B. Zhang, S. Wang, A. Hayik, G. Roitberg, K.F. Seabra, F. Wong, X. Paesani, S. Wu, V. Brozell, H. Tsui, L. Gohlke, C. Yang, J. Tan, V. Mongan, G. Hornak, P. Cui, D.H. Beroza, C. Mathews, W.S.R. Schafmeister, P.A. Kollman, AMBER 9, University of California, San Francisco, 2006.
- [45] Y. Duan, C. Wu, S. Chowdhury, M.C. Lee, G. Xiong, W. Zhang, R. Yang, P. Cieplak, R. Luo, T. Lee, A point-charge force field for molecular mechanics simulations of proteins, *J. Comput. Chem.* 24 (2003) 1999–2012.
- [46] J. Wang, R.M. Wolf, J.W. Caldwell, P.A. Kollman, D.A. Case, Development and testing of a general Amber force field, *J. Comput. Chem.* 25 (2004) 1157–1174.
- [47] G. Mukherjee, N. Patra, P. Barua, B. Jayaram, A fast empirical GAFF compatible partial atomic charge assignment scheme for modeling interactions of small molecules with biomolecular targets, *J. Comput. Chem.* 32 (2011) 893–907.
- [48] M.J. Frisch, G.W. Trucks, H.B. Schlegel, G.E. Scuseria, M.A. Robb, J.R. Cheeseman, J.A. Montgomery Jr., T. Vreven, K.N. Kudin, J.C. Burant, J.M. Millam, S.S. Iyengar, J. Tomasi, V. Barone, B. Mennucci, M. Cossi, G. Scalmani, N. Rega, G.A. Petersson, H. Nakatsuji, M. Hada, M. Ehara, K. Toyota, R. Fukuda, J. Hasegawa, M. Ishida, T. Nakajima, Y. Honda, O. Kitao, H. Nakai, M. Klene, X. Li, J.E. Knox, H.P. Hratchian, J.B. Cross, C. Adamo, J. Jaramillo, R. Gomperts, R.E. Stratmann, O. Yazyev, A.J. Austin, R. Cammi, C. Pomelli, J.W. Ochterski, P.Y. Ayala, K. Morokuma, G.A. Voth, P. Salvador, J.J. Dannenberg, V.G. Zakrzewski, S. Dapprich, A.D. Daniels, M.C. Strain, O. Farkas, D.K. Malick, A.D. Rabuck, K. Raghavachari, J.B. Foresman, J.V. Ortiz, Q. Cui, A.G. Baboul, S. Clifford, J. Cioslowski, B.B. Stefanov, G. Liu, A. Liashenko, P. Piskorz, I. Komaromi, R.L. Martin, D.J. Fox, T. Keith, M.A. Al-Laham, C.-Y. Peng, A. Nanayakkara, M. Challacombe, P.M.W. Gill, B. Johnson, W. Chen, M.-W. Wong, C. Gonzalez, J.A. Pople, Gaussian 03, Gaussian, Inc., Wallingford, CT, 2003.
- [49] W.L. Jorgensen, J. Chandrasekhar, J.D. Madura, R.W. Impey, M.L. Klein, Comparison of single potential function for simulating liquid water, *J. Chem. Phys.* 79 (1983) 926–935.
- [50] T. Darden, D. York, L. Pedersen, Particle mesh Ewald: an $N \log(N)$ method for Ewald sums in large systems, *J. Chem. Phys.* 98 (1993) 10089–10094.
- [51] J.P. Ryckaert, G. Cicotti, H.J.C. Berendsen, Numerical integration of the Cartesian equations of motion of a system with constraints: molecular dynamics of n-alkanes, *J. Comput. Phys.* 23 (1977) 327–341.
- [52] X. Wu, B.R. Brooks, Self-guided Langevin dynamics simulation method, *Chem. Phys. Lett.* 381 (2003) 518–521.
- [53] B.P. Ling, L.H. Dong, R. Zhang, Z.G. Wang, Y.J. Liu, C.B. Liu, Theoretical studies on the interaction of XIAP–BIR3 domain with bicyclic and tricyclic core monovalent Smacmimetics, *J. Mol. Graph. Model.* 29 (2010) 354–362.
- [54] Y. Yang, J. Qin, H. Liu, X. Yao, Molecular dynamics simulation free energy calculation and structure-based 3D-QSAR studies of B-Raf kinase inhibitors, *J. Chem. Inf. Model.* 50 (2011) 1574–1588.
- [55] T. Hou, J. Wang, Y. Li, W. Wang, Assessing the performance of the molecular mechanics/Poisson Boltzmann surface area and molecular mechanics/generalized Born surface area methods. II. The accuracy of ranking poses generated from docking, *J. Comput. Chem.* 32 (2011) 866–877.
- [56] T. Hou, J. Wang, Y. Li, W. Wang, Assessing the performance of the MM/PBSA and MM/GBSA methods. I. The accuracy of binding free energy calculations based on molecular dynamics simulations, *J. Chem. Inf. Model.* 51 (2011) 69–82.
- [57] L. Saiz-Urra, M.A. Cabrera, M. Froeyen, Exploring the conformational changes of the ATP binding site of gyrase B from *Escherichia coli* complexed with different established inhibitors by using molecular dynamics simulation. Protein–ligand interactions in the light of the alanine scanning and free energy decomposition methods, *J. Mol. Graph. Model.* 29 (2011) 726–739.
- [58] N.M. Micalo, A.L. Macedo, B.J. Goodfellow, V. Felix, Tetrapyrrole binding affinity of the murine and human p22HBP heme-binding proteins, *J. Mol. Graph. Model.* 29 (2010) 396–405.
- [59] D.A. Case, T.E. Cheatham, T. Darden, H. Gohlke, R. Luo, K.M. Merz, A. Onufriev, C. Simmerling, B. Wang, R.J. Woods, The Amber biomolecular simulation program, *J. Comput. Chem.* 26 (2005) 1668–1688.
- [60] Y. Ding, Y. Mei, J.Z.H. Zhang, Quantum mechanical studies of residue-specific hydrophobic interaction in p53–MDM2 binding, *J. Phys. Chem. B* 112 (2008) 11396–11401.
- [61] L.T. Chong, Y. Duan, L. Wang, I. Massova, P.A. Kollman, Molecular dynamics and free-energy calculations applied to affinity maturation in antibody 48G7, *Proc. Natl. Acad. Sci. U.S.A.* 96 (1999) 14330–14335.
- [62] B. Kuhn, P.A. Kollman, Binding of a diverse set of ligands to avidin and streptavidin: an accurate quantitative prediction of their relative affinities by a combination of molecular mechanics and continuum solvation models, *J. Med. Chem.* 43 (2000) 3786–3791.
- [63] S. Huo, J. Wang, P. Cieplak, P.A. Kollman, I.D. Kuntz, Molecular dynamics and free energy analyses of cathepsin D–inhibitor interactions: insights into structure-based ligand design, *J. Med. Chem.* 45 (2002) 1412–1419.
- [64] I. Massova, P.A. Kollman, Computational alanine scanning to probe protein–protein interactions: a novel approach to evaluate binding free energies, *J. Am. Chem. Soc.* 121 (1999) 8133–8143.
- [65] G.W. Yu, M. Vaysburd, M.D. Allen, G. Settanni, A.R. Fersht, Structure of human MDM4 N-terminal domain bound to a single-domain antibody, *J. Mol. Biol.* 385 (2009) 1578–1589.
- [66] I.S. Moreira, P.A. Fernandes, M.J. Ramos, Protein–protein recognition: a computational mutagenesis study of the MDM2–P53 complex, *Theor. Chem. Acc.* 120 (2008) 533–542.
- [67] B. Ma, R. Nussinov, Trp/Met/Phe hot spots in protein–protein interactions: potential targets in drug design, *Curr. Top. Med. Chem.* 7 (2007) 999–1005.
- [68] L.M. Espinoza-Fonseca, J. García-Machorro, Aromatic–aromatic interactions in the formation of the MDM2–p53 complex, *Biochem. Biophys. Res. Commun.* 370 (2008) 547–551.
- [69] A.C. Wallace, R.A. Laskowski, J.M. Thornton, LIGPLOT: a program to generate schematic diagrams of protein–ligand interactions, *Protein Eng.* 8 (1995) 127–134.
- [70] K. Sakurai, C. Schubert, D. Kahne, Crystallographic analysis of an 8-mer p53 peptide analogue complexed with MDM2, *J. Am. Chem. Soc.* 128 (2006) 11000–11001.
- [71] C. Riedinger, J.M. McMonnell, Inhibitors of MDM2 and MDMX: a structural perspective, *Future Med. Chem.* 1 (2009) 1075–1094.